Global stability of base and mean flows: a general approach and its applications to cylinder and open cavity flows

DENIS SIPP AND ANTON LEBEDEV

ONERA, 8 rue des Vertugadins, 92190 Meudon, France

This article deals with the first Hopf bifurcation of a cylinder flow, and more particularly with the properties of the unsteady periodic Kármán vortex street regime that sets in for supercritical Reynolds numbers $Re > 46$. Barkley (*Europhys. Lett.* vol. 75, 2006, p. 750) has recently studied the linear properties of the associated mean flow, i.e. the flow which is obtained by a time average of this unsteady periodic flow. He observed, thanks to a global mode analysis, that the mean flow is marginally stable and that the eigenfrequencies associated with the global modes of the mean flow fit the Strouhal to Reynolds experimental function well in the range $46 < Re < 180$. The aim of this article is to give a theoretical proof of this result near the bifurcation. For this, we do a global weakly nonlinear analysis valid in the vicinity of the critical Reynolds number Re_c based on the small parameter $\epsilon = Re_c^{-1} - Re^{-1} \ll 1$. We compute numerically the complex constants λ and μ' which appear in the Stuart–Landau amplitude equation: $\mathrm{d}A/\mathrm{d}t = \epsilon \lambda A - \epsilon \mu' A |A|^2$. Here A is the scalar complex amplitude of the critical global mode. By analysing carefully the nonlinear interactions yielding the term μ', we show for the cylinder flow that the mean flow is approximately marginally stable and that the linear dynamics of the mean flow yields the frequency of the saturated Stuart–Landau limit cycle. We will finally show that these results are not general, by studying the case of the bifurcation of an open cavity flow. In particular, we show that the mean flow in this case remains strongly unstable and that the frequencies associated with the eigenmodes do not exactly match those of the nonlinear unsteady periodic cavity flow. It will be demonstrated that two precise conditions must hold for a linear stability analysis of a mean flow to be relevant and useful.

1. Introduction

The prediction of the frequency of globally unstable flows has recently received much attention. In the framework of weakly non-parallel flows, linear (see Monkewitz, Huerre & Chomaz 1993) and fully nonlinear criteria (see Pier & Huerre 2001) have successively been built to predict this frequency. In the case of wake flows, Hammond & Redekopp (1997) and Pier (2002) have noticed that a linear criterion applied to the mean flow, and not to the base flow, yields particularly good results for the prediction of the frequency of the unsteadiness. Barkley (2006) confirmed this result thanks to a global linear stability analysis, and showed in addition that the mean flow was marginally stable. These two results are illustrated for the cylinder flow in figure 1. Figures 1(*a*) and 1(*b*), respectively, represent the pulsation and amplification rate of the eigenmodes as a function of the Reynolds number. The results concerning the base flow are shown by dotted lines, while those for the mean flow are given by triangles. We have also sketched the experimental pulsation obtained by Williamson (1988)
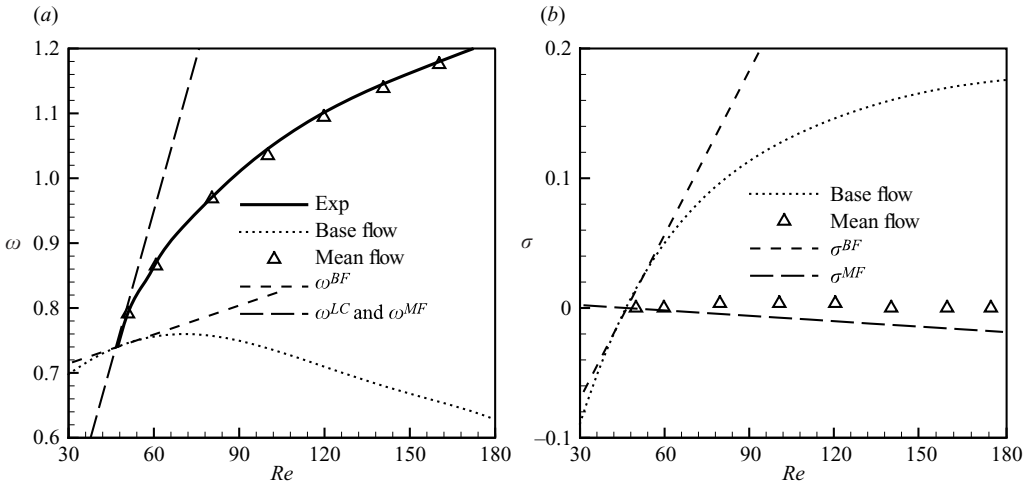
FIGURE 1. Cylinder flow. (*a*) Pulsation ω against Reynolds number Re. The solid line represents the experimental results of Williamson (1988). The dotted line sketches the pulsations obtained by Barkley (2006), thanks to linear global stability analyses applied to the base flows. The triangles, also from Barkley (2006), refer to analogous calculations applied to the mean flows. The dashed line represents ω^{BF} as defined in (2.29), while the long-dashed line represents ω^{LC} and ω^{MF} as defined in (2.35) and (2.45). (*b*) The same information as in (*a*), but for the amplification rate σ. Note that there is no solid line representing experimental data and that the long-dashed line only represents σ^{MF} since σ^{LC} is not defined.

using a solid line in figure 1(*a*). It clearly appears that in figure 1(*a*) the triangles closely follow the experimental data for the pulsation, i.e. the mean flow calculations yield the true nonlinear frequency, and that in figure 1(*b*) the triangles are located on the horizontal axis for the amplification rate, i.e. the mean flow is stable. The aim of this article is to give a theoretical justification of these two observations thanks to a global weakly nonlinear analysis valid in the vicinity of the critical Reynolds number. More precisely, the final outcome of this paper will be a condition for the mean flow to be stable and for the mean flow eigenfrequencies to match the experimental ones.

The present article is based on a weakly nonlinear stability analysis performed in a global framework, i.e. the unknowns depend on two spatial coordinates x and y. From a historical point of view, Jackson (1987) and Zebib (1987) were the first to approach the linear stability problem globally. In the case of the cylinder flow, several authors, including Ding & Kawahara (1999), Barkley (2006) and Giannetti & Luchini (2007), revisited the linear stability of this flow recently. The idea of performing a weakly nonlinear stability analysis in a global framework has been suggested by Chomaz (2005). By the way, it is interesting to note that a weakly nonlinear analysis is ill-posed in the case of a weakly non-parallel flow (see Le Dizès, Huerre & Chomaz 1993) and that it is well-posed again in the strongly non-parallel case, i.e. in the global framework.

The paper is organized as follows. Section 2 is devoted to the cylinder flow and to the derivation of the two conditions that exist for a mean flow to be approximately marginally stable and for the mean flow eigenfrequencies to match the true frequencies of the unsteadiness. We will show that these conditions are satisfied in the case of the cylinder flow. In §3 we demonstrate that these conditions are not satisfied for all globally unstable open flows by considering a counter-example, i.e. the case of an open cavity flow.
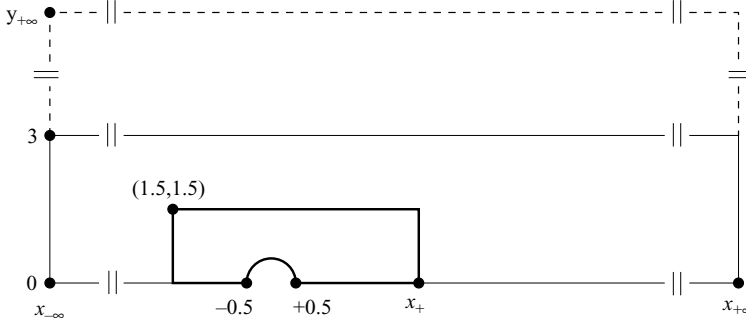
FIGURE 2. Mesh structure for the cylinder flow: $x_{-\infty}$, $x_{+\infty}$ and $y_{+\infty}$ are, respectively, the location of the inlet, outlet and transverse boundaries. The thick solid line, the thin solid line and the dashed line are, respectively, characterized by the vertex densities n_1, n_2 and n_3; x_+ is the downstream location of the region meshed with the n_1 vertex density.

2. The case of the cylinder

2.1. *Geometry*

We consider a cylinder of diameter D in a uniform flow of velocity U_∞. In the following, all quantities are made non-dimensional using these reference length and velocity scales. The two-dimensional incompressible Navier–Stokes equations then read:

$$\partial_t \boldsymbol{u} + \nabla \boldsymbol{u} \cdot \boldsymbol{u} + \nabla p - Re^{-1} \Delta \boldsymbol{u} = 0 \quad \text{and} \quad \nabla^T \boldsymbol{u} = 0, \tag{2.1}$$

where $(\boldsymbol{u}, p)$ represent the velocity and pressure of the flow field and Re is the Reynolds number based on D and U_∞. Note that ^{T} designates the transpose, so that $\nabla^T \boldsymbol{u}$ represents the divergence of the flow field $\boldsymbol{u}$. We use a Cartesian coordinate system (x, y) whose origin is located at the centre of the cylinder. The longitudinal and transverse velocities are denoted $\boldsymbol{u} = (u \ v)^T$. The configuration is shown in figure 2. The upstream $\partial \Omega_1$, downstream $\partial \Omega_3$ and upper boundary $\partial \Omega_4$ are located respectively at $x = x_{-\infty}$, $x = x_{+\infty}$ and $y = y_{+\infty}$. We use Dirichlet boundary conditions $(u, v) = (1, 0)$ on the inlet $\partial \Omega_1$, no-slip boundary conditions $(u, v) = (0, 0)$ on the cylinder boundary $\partial \Omega_0$, symmetric boundary conditions $(\partial_y u = 0, v = 0)$ on the upper boundary $\partial \Omega_4$ and outflow boundary conditions on the outlet $\partial \Omega_3$. Note that we only consider the domain $y \geqslant 0$, the boundary $\partial \Omega_0$ representing the upper half of the cylinder and $\partial \Omega_2$ the symmetry plane.

For the spatial discretizations, we use Taylor–Hood ($P2, P2, P1$) finite elements to represent the unknowns (u, v, p). Six different meshes, denoted C1 to C6, have been used, which exhibit various spatial extents and various vertex densities. The spatial extents of the meshes are governed by the parameters $x_{-\infty}$, $x_{+\infty}$ and $y_{+\infty}$, while the vertex densities are fixed by the parameters x_+, n_1, n_2 and n_∞. The three last parameters are the number of vertices per unit length on some particular curves. On the thick solid curve in figure 2, the size of the triangle sides is equal to $1/n_1$, on the thin solid curve it is equal to $1/n_2$, and on the dashed curve to $1/n_\infty$. Here x_+ is the downstream abscissa of the region meshed by the n_1 vertex density. These parameters are given for all meshes in table 1. C1 and C2 have the same spatial extent but have different vertex densities. C1 and C4 have the same vertex densities but the downstream boundary $x_{+\infty}$ is moved. In the same spirit, C1 and C5 differ by the position of the upstream boundary $x_{-\infty}$, while C1 and C6 have a different transverse boundary position $y_{+\infty}$. C3 has a maximal vertex density with upstream

Mesh	$x_{-\infty}$	$x_{+\infty}$	$y_{+\infty}$	x_+	n_1	n_2	n_3	n_t	$n_{\text{d.o.f.}}$
C1	−60	200	30	1.5	24	7	1	190868	864514
C2	−60	200	30	10.0	24	11	1	409955	1853313
C3	−60	100	30	50.0	37	11	1	462635	2090363
C4	−60	175	30	1.5	24	7	1	172034	779261
C5	−30	200	30	1.5	24	7	1	167038	756679
C6	−60	200	25	1.5	24	7	1	173776	787575

TABLE 1. Cylinder flow. Different meshes used with characteristic parameters: $x_{-\infty}$, $x_{+\infty}$ and $y_{+\infty}$ are, respectively, the location of the inlet, outlet and transverse boundaries; n_1, n_2 and n_3, respectively, designate the vertex densities on the thick solid line, the thin solid line and the dashed line presented in figure 2; x_+ is the downstream location of the region meshed with the n_1 vertex density; n_t is the number of triangles, while $n_{\text{d.o.f.}}$ is the number of degrees of freedom of an unknown (u, v, p). The meshes C1 and C2 have the same spatial extent but with different vertex densities. C1 and C4 have the same vertex densities but with a different location of the outlet boundary. In the same way, C1 and C5 differ by the location of the inlet boundary, while C1 and C6 differ by the location of the transverse boundary.

and transverse boundaries located as in C1 and C2. Table 1 also includes the number of triangles n_t and the number of degrees of freedom $n_{\text{d.o.f.}}$ to represent the unknowns (u, v, p). Hence, in the following, $n_{\text{d.o.f.}}$ is the size of the various matrices. Note that all matrices are built thanks to the FreeFEM++ software (see www.freefem.org), while all matrix inverses are handled using the UMFPACK library, which uses a sparse direct LU solver based on an unsymmetric-pattern multifrontal method (see Davis & Duff 1997; Davis 2004).

In the following, we will focus on mesh C1 to present all results. A comparison of the results obtained with the meshes C1 to C6 is given in Appendix A.

2.2. *Presentation of the weakly nonlinear analysis*

The Reynolds number Re is chosen to be very close and slightly above the critical Reynolds number Re_c where the first bifurcation occurs:

$$Re^{-1} = Re_c^{-1} - \epsilon \tag{2.2}$$

with $0 < \epsilon \ll 1$. In the following, we will perform a multiple time scale analysis based on the 'fast' time scale t and the 'slow' time scale $t_1 = \epsilon t$. We consider the following asymptotic expansion of the flow field $\boldsymbol{U} = (u\ v\ p)^T$ with the small parameter ϵ:

$$\boldsymbol{U}(t) = \boldsymbol{U}_0 + \sqrt{\epsilon}\boldsymbol{U}_1(t, t_1) + \epsilon\boldsymbol{U}_2(t, t_1) + \epsilon\sqrt{\epsilon}\boldsymbol{U}_3(t, t_1) + \cdots. \tag{2.3}$$

Note that $\boldsymbol{U}_0$ is a steady flow which is symmetric in y, i.e. $\partial_t \boldsymbol{U}_0 = \partial_{t_1} \boldsymbol{U}_0 = 0$ on the whole domain and $(\partial_y u_0 = 0, v_0 = 0)$ on $\partial\Omega_2$. It corresponds to the flow that is observed around the cylinder at the critical Reynolds number $Re = Re_c$. This expansion is introduced in the Navier–Stokes equations (2.1) with the Reynolds number given in (2.2) in terms of ϵ. For small ϵ, we obtain a series of equations at various orders in $\sqrt{\epsilon}^i$.

(i) At order $\sqrt{\epsilon}^0$, we are faced with a nonlinear equation specifying that $\boldsymbol{U}_0$ is a solution of the steady Navier–Stokes equations at the critical Reynolds number Re_c.

(ii) At order $\sqrt{\epsilon}^1$, we obtain an eigenproblem specifying that $\boldsymbol{U}_1$ may be taken as a superposition of global modes of the steady flow field $\boldsymbol{U}_0$. We can therefore choose that $\boldsymbol{U}_1$ be the critical eigenmode multiplied by a scalar amplitude A.

(iii) At order $\sqrt{\epsilon}^2$ we obtain inhomogeneous linear non-degenerate equations that may readily be solved.

(iv) At order $\sqrt{\epsilon}^3$, we obtain similar linear inhomogeneous equations, except that some of them are degenerate. Hence, compatibility conditions for the associated forcing terms have to be enforced in order for these equations to have a solution. These conditions will yield the 'slow' time scale behaviour of the complex scalar amplitude $A(t_1)$: $dA/dt_1 = \lambda A - (\mu + \nu)A|A|^2$, where λ, μ and ν are three complex constants whose meanings and values will be given in the next sections. This is a Stuart–Landau amplitude equation which may be re-written as

$$\frac{dA}{dt} = \epsilon \lambda A - \epsilon(\mu + \nu)A|A|^2. \tag{2.4}$$

In the next section, we will successively solve the equations at each order $\sqrt{\epsilon}^i$. Note that the Hopf bifurcation and the associated Stuart–Landau amplitude equation have already been introduced for the cylinder flow by Provansal, Mathis & Boyer (1987) and Dusek, Le Gal & Fraunie (1994). Both articles try to evaluate the Landau constants, Provansal *et al.* (1987) by means of an experiment and Dusek *et al.* (1994) by means of a direct numerical simulation performed at $Re = 48$. But these articles did not consider A as the amplitude of a global structure but only as a scalar variable (like a velocity component) taken at some particular point in the flow. Hence, their coefficients are relative to a particular point in space and to a particular variable. The present approach is global in nature. Once one knows the spatial structure of the critical global mode and the value of the Stuart–Landau coefficients presented above, one readily obtains, for every point in the spatial domain, the Stuart–Landau coefficients governing any variable. Finally, let us recall that the present approach is only valid in the vicinity of the bifurcation, i.e. for Reynolds numbers Re which are very close to Re_c.

2.3. *Weakly nonlinear analysis*

2.3.1. *Order $\sqrt{\epsilon}^0$*

At order $\sqrt{\epsilon}^0$, we obtain the following nonlinear equation for $\boldsymbol{U}_0$ (recall that $\boldsymbol{U}_0 = (u_0, v_0, p_0)^T$ and $\boldsymbol{u}_0 = (u_0, v_0)^T$):

$$\nabla \boldsymbol{u}_0 \cdot \boldsymbol{u}_0 + \nabla p_0 - Re_c^{-1}\Delta \boldsymbol{u}_0 = 0 \text{ and } \nabla^T \boldsymbol{u}_0 = 0, \tag{2.5}$$

with Dirichlet boundary conditions $(u_0, v_0) = (1, 0)$ on the inlet $\partial\Omega_1$, no-slip boundary conditions $(u_0, v_0) = (0, 0)$ on the cylinder boundary $\partial\Omega_0$, symmetric boundary conditions $(\partial_y u_0 = 0, v_0 = 0)$ on the symmetry plane $\partial\Omega_2$ and on the upper boundary $\partial\Omega_4$, and outflow boundary conditions $(p_0 - Re_c^{-1}\partial_x u_0 = 0, \partial_x v_0 = 0)$ on the outlet $\partial\Omega_3$. These nonlinear equations for $\boldsymbol{U}_0$ are solved using an iterative Newton method. For this, we go through the following steps:

(*a*) Find an approximate guess solution $\boldsymbol{U}$ which satisfies the above boundary conditions. For example, this guess solution may be obtained by a few time steps of a Direct Numerical Simulation of equations (2.1).

(*b*) Solve for $\delta \boldsymbol{U} = (\delta u \ \delta v \ \delta p)^T$ in

$$\begin{pmatrix} \nabla() \cdot \boldsymbol{u} + \nabla \boldsymbol{u} \cdot () - Re_c^{-1}\Delta & \nabla \\ \nabla^T & 0 \end{pmatrix} \begin{pmatrix} \delta \boldsymbol{u} \\ \delta p \end{pmatrix} = -\begin{pmatrix} \nabla \boldsymbol{u} \cdot \boldsymbol{u} + \nabla p - Re_c^{-1}\Delta \boldsymbol{u} \\ \nabla^T \boldsymbol{u} \end{pmatrix}. \tag{2.6}$$

For this linear problem, we impose homogeneous Dirichlet boundary conditions on the inlet $\partial\Omega_1$ and on the cylinder boundary $\partial\Omega_0$, symmetric boundary conditions
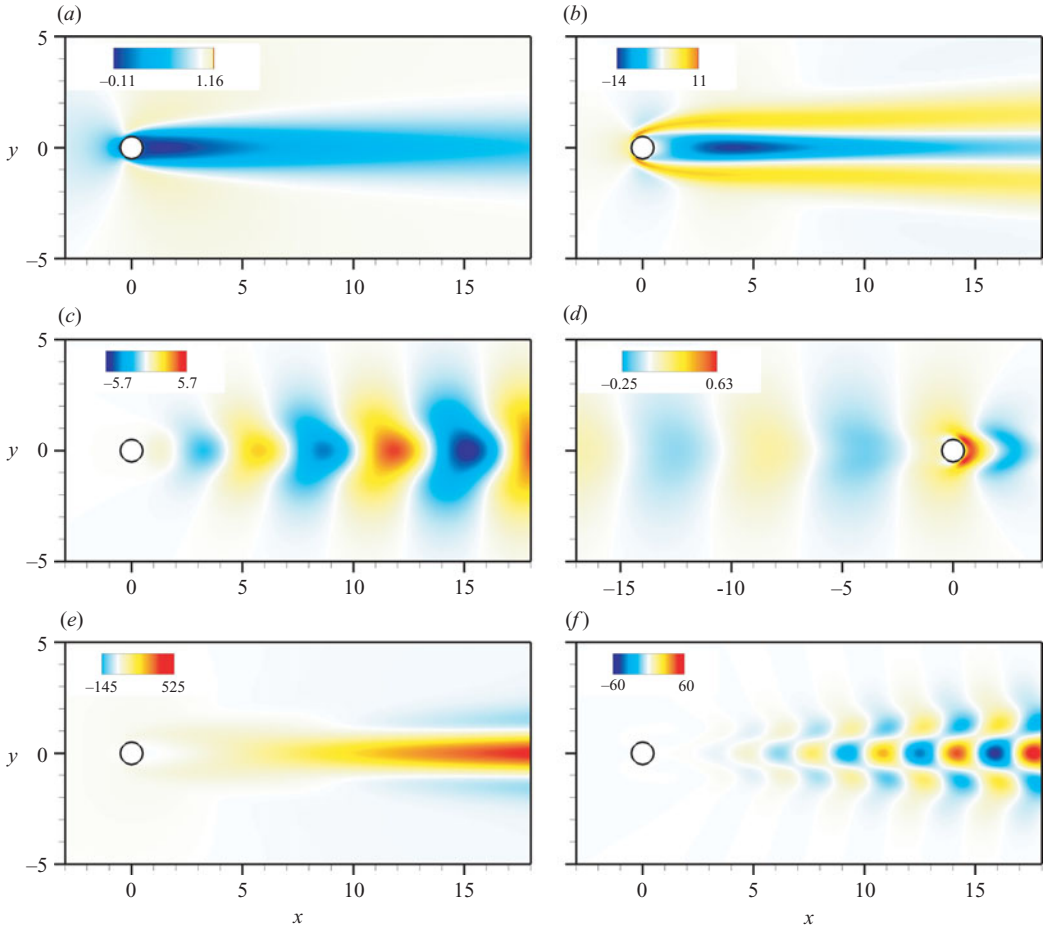
FIGURE 3. Cylinder flow at $Re_c = 46.6$. Representation of the various flow fields appearing at each order in the weakly nonlinear analysis. Mesh C1. Only a small portion of the full computational domain is shown, (a) base flow u_0, (b) base flow modification u_2^1 due to an ϵ Reynolds increase, (c) first harmonic $\mathrm{Re}(v_1^A)$, (d) corresponding adjoint eigenmode $\mathrm{Re}(\hat{v}_1^A)$, (e) zeroth (mean flow) harmonic $u_2^{|A|^2}$, (f) second harmonic $\mathrm{Re}(u_2^{A^2})$.

on the symmetry plane $\partial\Omega_2$ and on $\partial\Omega_4$. On the left-hand side, we recognize the steady Navier–Stokes operator linearized around U and on the right-hand side, the residual of the steady Navier–Stokes equations for U. This is an inhomogeneous non-degenerate linear problem which may readily be solved.

(c) Set $U = U + \delta U$.

(d) If $\sqrt{\int_\Omega (\delta u^2 + \delta v^2)\mathrm{d}x\mathrm{d}y} > 10^{-14}$ (machine precision), go to step (b).

(e) Set $U_0 = U$.

In practice, only few iterations, e.g. typically 7 or 8, are needed to converge the solution of equation (2.5) to machine precision. For $Re = 46.6$, the solution of this nonlinear equation is represented in figure 3(a). As expected, we observe a large recirculation region developing in the wake of the cylinder with negative values of the longitudinal velocity attaining $u_0 = -0.11$. In addition, the longitudinal velocity
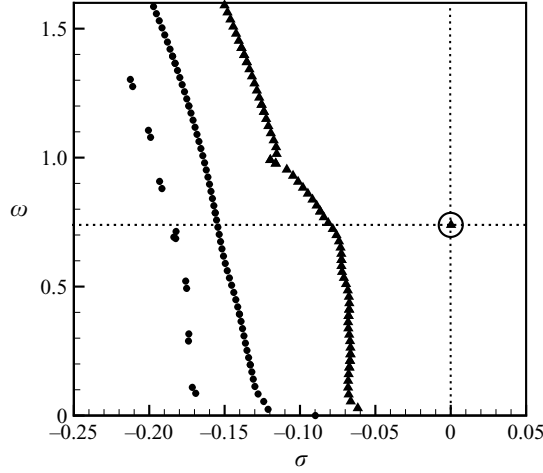
FIGURE 4. Eigenvalues of the cylinder flow in the (σ, ω) plane at $Re = 46.6$. Mesh C1. A marginally stable eigenmode exists for $\omega = 0.74$ (see the circled triangle). The filled triangles represent antisymmetric modes and the filled circles symmetric modes.

u_0 on the symmetry plane is shown in figure 5(b) by a dotted line. We can see that the recirculation length is equal to 3.2, which is typical for this Reynolds number.

2.3.2. *Order $\sqrt{\epsilon}^1$*

At order $\sqrt{\epsilon}^1$, we obtain the following homogeneous equation determining U_1:

$$(\partial_t \mathscr{L} + \mathscr{M}) U_1 = 0 \tag{2.7}$$

with the linear operators:

$$\mathscr{L} = \begin{pmatrix} \mathscr{I} & 0 \\ 0 & 0 \end{pmatrix}, \quad \mathscr{M} = \begin{pmatrix} \nabla() \cdot u_0 + \nabla u_0 \cdot () - Re_c^{-1}\Delta & \nabla \\ \nabla^T & 0 \end{pmatrix} \tag{2.8}$$

Focusing on the global normal modes, we look for eigenvalues $\sigma + i\omega$ associated to eigenvectors U such that: $\mathscr{M}U = -(\sigma + i\omega)\mathscr{L}U$. Introducing the linear operator

$$\mathscr{K}_\psi = \psi\mathscr{L} + \mathscr{M} = \begin{pmatrix} \psi\mathscr{I} + \nabla() \cdot u_0 + \nabla u_0 \cdot () - Re_c^{-1}\Delta & \nabla \\ \nabla^T & 0 \end{pmatrix} \tag{2.9}$$

this generalized eigenproblem may be written in the form: $\mathscr{K}_{\sigma+i\omega}U = 0$. Homogeneous boundary conditions are specified on the inlet $\partial\Omega_1$ and on the cylinder $\partial\Omega_0$, antisymmetric (resp. symmetric) boundary conditions ($u = 0$, $\partial_y v = 0$) (resp. ($\partial_y u = 0$, $v = 0$)) on the symmetry plane $\partial\Omega_2$ for antisymmetric (resp. symmetric) modes. On the outlet $\partial\Omega_3$, we specify outflow boundary conditions: ($p - Re_c^{-1}\partial_x u = 0$, $\partial_x v = 0$). This problem is solved thanks to an Arnoldi method based on a shift-invert strategy (ARPACK library). In figure 4, the eigenvalues are displayed for $Re = 46.6$ in the (σ, ω) plane, filled triangles (resp. filled circles) representing antisymmetric (resp. symmetric) modes. Only the domain $\omega \geqslant 0$ has been shown, since the plot is symmetric with respect to $\omega = 0$: if $\mathscr{K}_{\sigma+i\omega}U = 0$, then $\mathscr{K}_{\sigma-i\omega}\overline{U} = 0$. We can see that there exists an antisymmetric eigenvector which is marginally stable for $\omega = 0.74$. This particular eigenvalue will be denoted by ω_0, and the associated eigenvector by U_1^A so that

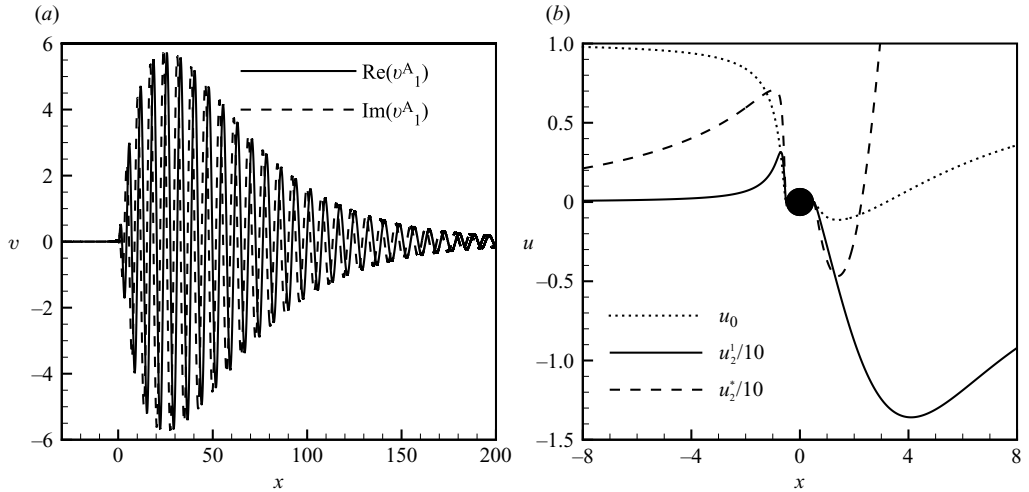$$\mathscr{K}_{i\omega_0}U_1^A = 0. \tag{2.10}$$

FIGURE 5. Cylinder flow at $Re_c = 46.6$. Mesh C1. (*a*) The first harmonic is described through the real and imaginary parts of the transverse velocity v_1^A on the symmetry plane. The eigenmode experiences a dramatic increase in strength in the region $0 < x < 25$ before slowly decaying. The real and imaginary parts are analogous and are approximately 1/4 spatial period out of phase, which enables a continuous downstream convection of the vortical structures. (*b*) Longitudinal velocity on the symmetry plane for the base flow u_0 (dotted line), for the base flow modification u_2^1 and for the mean flow modification u_2^*. The base flow exhibits a recirculation extending up to $x = 3.2$. The base flow modification u_2^1 tends to lengthen this region since $u_2^1 < 0$ for $x > 0$. The mean flow modifications on the contrary tend to reduce this length since $u_2^* > 0$ for $x > 2.25$.

Note also that 0 and $2i\omega_0$ are not eigenvalues in figure 4, so that $\mathcal{K}_0$ and $\mathcal{K}_{2i\omega_0}$ are non-degenerate linear operators, i.e $\mathcal{K}_0^{-1}$ and $\mathcal{K}_{2i\omega_0}^{-1}$ exist. The existence of $\mathcal{K}_0^{-1}$ also justifies the validity of the Newton method used in §2.3.1, since the linear operator in (2.6) is equal to $\mathcal{K}_0$ for the last Newton iterations.

The real part of the transverse velocity of the eigenmode v_1^A is represented in figure 3(*c*). It represents an array of counter-rotating vortices which develop in the wake of the cylinder. In figure 5(*a*), we show the corresponding real and imaginary parts of the transverse velocity on the symmetry plane. We can see that they are approximately 1/4 spatial period out of phase, which enables a continuous downstream convection of the vortical structures. We also observe that the eigenmode strengthens in the near-wake of the cylinder and reaches a maximum for $x \approx 25$. Downstream of this location, the eigenmode continuously loses its energy and slowly vanishes. This may be explained by considering the longitudinal velocity of the base flow u_0 on the symmetry plane, which is represented in figure 5(*b*) with dotted lines. We notice that the velocity deficit, which is responsible for the instability, is maximum in the near-wake and then slowly decreases due to viscous diffusion. Note that these descriptions are in agreement with the experimental and numerical study of Wesfreid, Goujon-Durand & Zielinska (1996), who analysed the structure of the global mode in the wake of a trapezoidal and a triangular-shaped cylinder.

In the following, we choose for $\boldsymbol{U}_1$:

$$\boldsymbol{U}_1 = A\mathrm{e}^{\mathrm{i}\omega_0 t}\boldsymbol{U}_1^A + \mathrm{c.c.}, \tag{2.11}$$

where A is a complex scalar which depends on the 'slow' time scale $t_1 = \epsilon t$ according to (2.4) and c.c. designates the complex conjugate. This flow field is also termed the first harmonic or critical eigenmode in the literature. The superscript ^{A} in (2.11) refers to the amplitude A of the structure U_1^A.

Note also that we use the following normalization condition for U_1^A: $v_1^A(1,0) = 0.4612$. This normalization condition seems odd *a priori*, but it has an advantage that we briefly explain here. It may be shown that the complex constant λ introduced in (2.4) is independent of the normalization, while μ and ν strongly depend on it. Hence, if U_1^A is multiplied by $\alpha e^{i\beta}$, then λ remains unchanged while μ and ν are both multiplied by α^2. This degree of freedom on the normalization of the eigenvector U_1^A is used here, i.e. the precise choice of the value 0.4612, so as to achieve $\lambda_r \approx \mu_r + \nu_r$. This normalization comes out naturally when studying the saturated limit cycle of the bifurcation (see § 2.4.2).

2.3.3. *Order* $\sqrt{\epsilon}^2$

At order $\sqrt{\epsilon}^2$, we obtain the following inhomogeneous linear equation determining U_2:

$$(\partial_t \mathscr{L} + \mathscr{M})U_2 = F_2^1 + |A|^2 F_2^{|A|^2} + (A^2 e^{2i\omega_0 t} F_2^{A^2} + \text{c.c.}) \tag{2.12}$$

with

$$F_2^1 = \begin{pmatrix} -\Delta u_0 \\ 0 \end{pmatrix}, \tag{2.13a}$$

$$F_2^{|A|^2} = \begin{pmatrix} -\nabla u_1^A \cdot \overline{u_1^A} - \nabla \overline{u_1^A} \cdot u_1^A \\ 0 \end{pmatrix}, \tag{2.13b}$$

$$F_2^{A^2} = \begin{pmatrix} -\nabla u_1^A \cdot \nabla u_1^A \\ 0 \end{pmatrix}. \tag{2.13c}$$

Note again that superscripts are used to identify different terms according to their respective amplitude, e.g.^{1}, $^{|A|^2}$ and $^{A^2}$. The terms on the right-hand side of (2.12) are forcing terms. All the velocity fields involved in these forcing terms have been determined at lower orders, i.e. at order $\sqrt{\epsilon}^0$ for u_0 and at order $\sqrt{\epsilon}^1$ for u_1^A, and are therefore known here. We seek a form for U_2 that matches the structure of these forcing terms:

$$U_2 = U_2^1 + |A|^2 U_2^{|A|^2} + (A^2 e^{2i\omega_0 t} U_2^{A^2} + \text{c.c.}). \tag{2.14}$$

Introducing this relation in (2.12) and identifying analogous terms yields three equations determining U_2^1, $U_2^{|A|^2}$ and $U_2^{A^2}$:

$$\mathscr{K}_0 U_2^1 = F_2^1, \tag{2.15a}$$

$$\mathscr{K}_0 U_2^{|A|^2} = F_2^{|A|^2}, \tag{2.15b}$$

$$\mathscr{K}_{2i\omega_0} U_2^{A^2} = F_2^{A^2}, \tag{2.15c}$$

The three unknowns U_2^1, $U_2^{|A|^2}$ and $U_2^{A^2}$ are symmetric in y since all forcing terms are symmetric in y. On the other boundaries, we enforce boundary conditions analogous to those used in the previous section, in particular, homogeneous on the inlet $\partial\Omega_1$

and on the cylinder $\partial\Omega_0$. As already mentioned, the operators $\mathscr{K}_0$ and $\mathscr{K}_{2i\omega_0}$ are non-degenerate since 0 and $2i\omega_0$ are not eigenvalues in figure 4. Hence, one may obtain the three unknowns from non-degenerate matrix inverses. The three unknowns may be interpreted in the following manner.

(i) U_2^1 consists of the base flow modifications related to the increase of the external control parameter $\epsilon > 0$. In other words, $U_0 + \epsilon U_2^1$ is a first-order approximation (in ϵ) of the base flow which exists at the Reynolds number $\epsilon > 0$. As expected, the forcing term F_2^1 corresponding to this flow field involves the Laplacian of the base flow U_0.

(ii) $|A|^2 U_2^{|A|^2}$ consists of the response of the flow to the steady nonlinear interactions involving the first harmonic, i.e. the interaction between the eigenmode $Ae^{i\omega_0 t}U_1^A$ and its conjugate. It is therefore a steady flow field, whose magnitude is proportional to $|A|^2$. It will be shown below that this flow field corresponds to the difference between the mean flow and the base flow. This term is also called the zeroth (mean flow) harmonic.

(iii) $A^2 e^{2i\omega_0 t}U_2^{A^2}$ consists of the response of the flow to the harmonic nonlinear interactions involving the first harmonic, i.e. the interaction of the eigenmode $Ae^{i\omega_0 t}U_1^A$ with itself. It is therefore a harmonic flow field characterized by the pulsation $2\omega_0$, whose magnitude is proportional to $|A|^2$. This term may also be called the second harmonic.

The longitudinal velocity fields u_2^1, $u_2^{|A|^2}$ and $\mathrm{Re}(u_2^{A^2})$ are represented in figures 3(b), 3(e) and 3(f). We can see that u_2^1 and $u_2^{|A|^2}$ display large structures characteristic of steady flows while $\mathrm{Re}(u_2^{A^2})$ exhibits small structures characteristic of harmonic flows. The combination of the real and imaginary parts of $U_2^{A^2}$ enables these small structures to be continuously convected downstream. A cut of the field u_2^1 along the symmetry plane is shown in figure 5(b) by a solid line. We notice that u_2^1 is always negative in the wake. Hence, an increase in Reynolds number yields an increase in the recirculation length for the base flow.

2.3.4. Order $\sqrt{\epsilon}^3$

At order $\sqrt{\epsilon}^3$, we obtain the following inhomogeneous linear equation determining U_3:

$$(\partial_t \mathscr{L} + \mathscr{M})U_3 = Ae^{i\omega_0 t}\left(-\lambda\mathscr{L}U_1^A + F_3^A\right) + A|A|^2 e^{i\omega_0 t}\left(\mu\mathscr{L}U_1^A + F_3^{A|A|^2}\right)$$

$$+ A|A|^2 e^{i\omega_0 t}\left(\nu\mathscr{L}U_1^A + F_3^{\bar{A}A^2}\right) + \text{c.c.} \quad +\cdots, \qquad (2.16)$$

with

$$F_3^A = \begin{pmatrix} -\nabla u_1^A \cdot \nabla u_2^1 - u_2^1 \cdot \nabla u_1^A - \Delta u_1^A \\ 0 \end{pmatrix}, \qquad (2.17a)$$

$$F_3^{A|A|^2} = \begin{pmatrix} -\nabla u_1^A \cdot \nabla u_2^{|A|^2} - u_2^{|A|^2} \cdot \nabla u_1^A \\ 0 \end{pmatrix}, \qquad (2.17b)$$

$$F_3^{\bar{A}A^2} = \begin{pmatrix} -\nabla\overline{u_1^A} \cdot \nabla u_2^{A^2} - u_2^{A^2} \cdot \nabla\overline{u_1^A} \\ 0 \end{pmatrix}, \qquad (2.17c)$$

On the right-hand side of (2.16), only the terms proportional to $e^{i\omega_0 t}$ have been given (many other terms do exist but are not useful here). The terms F_3^A, $F_3^{A|A|^2}$ and $F_3^{\bar{A}A^2}$ may readily be evaluated from calculations performed at lower orders. Note that

constants λ, μ and ν, which stem from the 'slow' time scale behaviour of A prescribed by equation (2.4), may be given any complex value at this stage of the analysis. As in §2.3.3, we seek a form for U_3 that matches the structure of the forcing terms:

$$U_3 = A\mathrm{e}^{\mathrm{i}\omega_0 t}U_3^A + A|A|^2\mathrm{e}^{\mathrm{i}\omega_0 t}U_3^{A|A|^2} + A|A|^2\mathrm{e}^{\mathrm{i}\omega_0 t}U_3^{\bar{A}A^2} + \text{c.c.} + \cdots. \tag{2.18}$$

Introducing this relation in (2.16) and equating analogous terms yields three equations governing the unknowns U_3^A, $U_3^{A|A|^2}$ and $U_3^{\bar{A}A^2}$:

$$\mathscr{K}_{\mathrm{i}\omega_0}U_3^A = -\lambda\mathscr{L}U_1^A + F_3^A, \tag{2.19a}$$

$$\mathscr{K}_{\mathrm{i}\omega_0}U_3^{A|A|^2} = \mu\mathscr{L}U_1^A + F_3^{A|A|^2}, \tag{2.19b}$$

$$\mathscr{K}_{\mathrm{i}\omega_0}U_3^{\bar{A}A^2} = \nu\mathscr{L}U_1^A + F_3^{\bar{A}A^2}. \tag{2.19c}$$

In these equations, all forcing terms are antisymmetric in y so that U_3^A, $U_3^{A|A|^2}$ and $U_3^{\bar{A}A^2}$ are also antisymmetric in y. The linear operator $\mathscr{K}_{\mathrm{i}\omega_0}$ is degenerate, and compatibility conditions have to be satisfied in order to determine U_3^A, $U_3^{A|A|^2}$ and $U_3^{\bar{A}A^2}$, which respectively determine λ, μ and ν. The unknowns may be interpreted in the following manner.

(i) $A\mathrm{e}^{\mathrm{i}\omega_0 t}U_3^A$ consists of the response of the flow to both the interaction of the first harmonic $A\mathrm{e}^{\mathrm{i}\omega_0 t}U_1^A$ with the base flow modification U_2^1, and to the viscous diffusion of the first harmonic. These interactions are responsible for the linear instability of the flow and determine the value of the complex constant λ.

(ii) $A|A|^2\mathrm{e}^{\mathrm{i}\omega_0 t}U_3^{A|A|^2}$ consists of the response of the flow to the interaction of the first harmonic $A\mathrm{e}^{\mathrm{i}\omega_0 t}U_1^A$ with the zeroth (mean flow) harmonic $|A|^2U_2^{|A|^2}$. This interaction yields the complex constant μ.

(ii) $A|A|^2\mathrm{e}^{\mathrm{i}\omega_0 t}U_3^{\bar{A}A^2}$ consists of the response of the flow to the interaction of the first harmonic $\bar{A}\mathrm{e}^{-\mathrm{i}\omega_0 t}\overline{U_1^A}$ with the second harmonic $A^2\mathrm{e}^{2\mathrm{i}\omega_0 t}U_2^{A^2}$. This interaction yields the complex constant ν.

In order to apply the compatibility conditions, let us introduce the scalar product

$$\langle U_\alpha, U_\beta\rangle = \iint_\Omega (\bar{u}_\alpha u_\beta + \bar{v}_\alpha v_\beta + \bar{p}_\alpha p_\beta)\mathrm{d}x\mathrm{d}y \tag{2.20}$$

and the linear operator

$$\hat{\mathscr{K}}_\psi = \begin{pmatrix} \bar{\psi}\mathscr{I} - \nabla()\cdot u_0 + (\nabla u_0)^T\cdot() - Re_c^{-1}\Delta & -\nabla \\ \nabla^T & 0 \end{pmatrix}. \tag{2.21}$$

It can be shown that for all flow fields U_α and U_β which are homogeneous on the inlet $\partial\Omega_1$ and on the cylinder $\partial\Omega_0$, symmetric on the upper boundary $\partial\Omega_4$, antisymmetric in y, we have

$$\langle U_\alpha, \mathscr{K}_\psi U_\beta\rangle = \langle \hat{\mathscr{K}}_\psi U_\alpha, U_\beta\rangle \tag{2.22}$$

This shows that $\hat{\mathscr{K}}_\psi$ is the adjoint operator to $\mathscr{K}_\psi$. Hence, as $\mathscr{K}_{\mathrm{i}\omega_0}$ is degenerate, $\hat{\mathscr{K}}_{\mathrm{i}\omega_0}$ should also be so. Therefore there exists $\hat{U}_1^A$ such that.

$$\hat{\mathscr{K}}_{\mathrm{i}\omega_0}\hat{U}_1^A = 0, \tag{2.23}$$

with the normalization condition $\hat{v}_1^A(1, 0) = 0.5$. Note that this normalization condition on the adjoint does not affect the values of λ, μ and ν and is therefore

not important. We nevertheless use it so that the computed adjoint is uniquely defined. Equation (2.23) is a generalized eigenproblem which is solved again thanks to the Arnoldi method. The adjoint vector $\hat{\boldsymbol{U}}_1^A$ associated with the eigenmode $\boldsymbol{U}_1^A$ is represented in figure 3(*d*). We notice that the adjoint is located in the region $x < 5$ and in particular in the upstream region of the cylinder. This has already been documented by Giannetti & Luchini (2007), and stems from the non-normality of the operator $\mathscr{K}_\psi$. As a matter of fact, looking at the definitions of $\mathscr{K}_\psi$ and $\hat{\mathscr{K}}_\psi$ we can see that the convection terms $\nabla()\cdot\boldsymbol{u}_0$ have opposite signs: the perturbations are convected downstream for $\mathscr{K}_\psi$ while they are convected upstream for $\hat{\mathscr{K}}_\psi$.

Applying the compatibility conditions then yields the value of the three complex constants λ, μ and ν:

$$\lambda = \frac{\langle \hat{\boldsymbol{U}}_1^A, \boldsymbol{F}_3^A \rangle}{\langle \hat{\boldsymbol{U}}_1^A, \mathscr{L}\boldsymbol{U}_1^A \rangle}, \quad \mu = -\frac{\langle \hat{\boldsymbol{U}}_1^A, \boldsymbol{F}_3^{A|A|^2} \rangle}{\langle \hat{\boldsymbol{U}}_1^A, \mathscr{L}\boldsymbol{U}_1^A \rangle}, \quad \nu = -\frac{\langle \hat{\boldsymbol{U}}_1^A, \boldsymbol{F}_3^{\bar{A}A^2} \rangle}{\langle \hat{\boldsymbol{U}}_1^A, \mathscr{L}\boldsymbol{U}_1^A \rangle}. \quad (2.24)$$

Numerically we obtain:

$$\lambda = 9.1 + 3.3\mathrm{i}, \quad \mu = 9.4 - 30\mathrm{i}, \quad \nu = -0.30 - 0.87\mathrm{i}. \quad (2.25)$$

We may compare the ratio $(\mu_i + \nu_i)/(\mu_r + \nu_r) \approx -3.4$ to the ratio -2.7 obtained by Dusek *et al.* (1994) by means of a direct numerical simulation at $Re = 48$. The discrepancy between these two values is not explained.

The integrands appearing in any of the scalar products involved in (2.24) are built from the product of an upstream located field, i.e. the adjoint $\hat{\boldsymbol{U}}_1^A$, and a downstream located field, i.e. $\boldsymbol{U}_1^A$, $\boldsymbol{F}_3^A$, $\boldsymbol{F}_3^{A|A|^2}$ and $\boldsymbol{F}_3^{\bar{A}A^2}$. Hence, the integrands are zero far upstream and downstream of the cylinder, which guarantees the convergence of these integrals. In order to analyse in more detail the spatial localization of these integrands, let us introduce the following complex functions depending on the abscissa x:

$$\lambda(x) = \frac{\langle \hat{\boldsymbol{U}}_1^A, \mathscr{P}_x\boldsymbol{F}_3^A \rangle}{\langle \hat{\boldsymbol{U}}_1^A, \mathscr{L}\boldsymbol{U}_1^A \rangle}, \mu(x) = -\frac{\langle \hat{\boldsymbol{U}}_1^A, \mathscr{P}_x\boldsymbol{F}_3^{A|A|^2} \rangle}{\langle \hat{\boldsymbol{U}}_1^A, \mathscr{L}\boldsymbol{U}_1^A \rangle}, \nu(x) = -\frac{\langle \hat{\boldsymbol{U}}_1^A, \mathscr{P}_x\boldsymbol{F}_3^{\bar{A}A^2} \rangle}{\langle \hat{\boldsymbol{U}}_1^A, \mathscr{L}\boldsymbol{U}_1^A \rangle}, \quad (2.26)$$

where $\mathscr{P}_x$ is a matrix step function:

$$\mathscr{P}_{x_0}(x, y) = \mathscr{I} \quad \text{if} \quad x \leqslant x_0 \quad (2.27a)$$
$$= 0 \quad \text{if} \quad x > x_0 \quad (2.27b)$$

Therefore, $\lambda(x_{-\infty}) = 0$ and $\lambda(x_{+\infty}) = \lambda$. Analogous properties hold for $\mu(x)$ and $\nu(x)$. These three functions have been represented in figure 6. We can see that all functions are roughly zero for $x < 0$. The function $\lambda(x)$ then abruptly increases within the region $0 < x < 7.5$, reaches a plateau and stays constant and equal to λ. Hence, the active region building λ is situated within $0 < x < 7.5$. The same phenomenon may be observed for functions $\mu(x)$ and $\nu(x)$, except that small oscillations are observed until $x \approx 50$. Hence, the active region building constants μ and ν extends far downstream, i.e. up to $x \approx 50$. To conclude, these two results imply the following in particular.

(i) To capture the linear instability, i.e. to achieve the convergence of the constant λ, the location of the outlet boundary should at least be equal to $x_{+\infty} = 7.5$.

(ii) To capture the nonlinear regime, i.e. to achieve a precise convergence of the nonlinear constants μ and ν, the location of the outlet boundary should at least be equal to $x_{+\infty} = 50$.
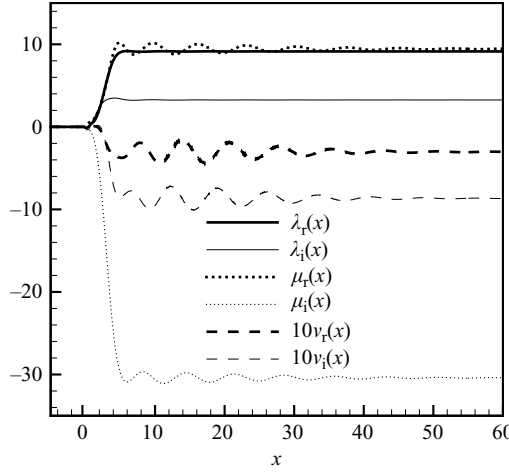
FIGURE 6. Cylinder flow at $Re_c = 46.6$. Mesh C1. The downstream convergence of the Landau constants is characterized by the evolution of the functions $\lambda(x)$, $\mu(x)$ and $\nu(x)$. We observe that the function $\lambda(x)$ attains its asymptotic value λ for $x \approx 7.5$ while the functions $\mu(x)$ and $\nu(x)$ experience small oscillations up to $x \approx 50$ before converging to μ and ν.

2.4. *Analysis of the amplitude equations*

The weakly nonlinear analysis has shown that the amplitude A of the critical global mode is governed by (2.4) with the numerical constants shown in (2.25). In this section, we analyse the behaviour of this equation in the linear and nonlinear regime. In particular, we will show that a saturated limit cycle exists at large times.

2.4.1. *Linear regime*

Considering the numerical values obtained in (2.25), we can see that $\mathrm{Re}(\lambda) > 0$ as expected, showing that the flow is linearly unstable for $\epsilon > 0$. For $|A| \ll 1$, only the linear part of the Stuart–Landau amplitude equation (2.4) remains: $\mathrm{d}A/\mathrm{d}t = \epsilon \lambda A$. Hence, $A(t) = A_0 \exp(\epsilon \lambda t)$ and $\boldsymbol{U} = \boldsymbol{U}_0 + \sqrt{\epsilon}[A_0 \exp(\mathrm{i}\omega_0 t + \epsilon \lambda t)\boldsymbol{U}_1^A + \mathrm{c.c.}] + \cdots$. The amplification rate and pulsation of the global mode of the base flow therefore reads

$$\sigma^{BF} = \epsilon \lambda_r, \quad \omega^{BF} = \omega_0 + \epsilon \lambda_i, \tag{2.28}$$

or, numerically,

$$\sigma^{BF} = 9.1\epsilon, \quad \omega^{BF} = 0.74 + 3.3\epsilon. \tag{2.29}$$

These two asymptotic relations are sketched with dashed lines in figures 1(*a*) and 1(*b*). As expected, the associated curves are tangent to the exact curves obtained by Barkley (2006) for the base flow stability calculations (dotted lines), which validates the present approach.

2.4.2. *Limit cycle*

We now study the dynamics of the full nonlinear amplitude equation (2.4). Setting $A = r\mathrm{e}^{\mathrm{i}\phi}$, we obtain

$$\frac{\mathrm{d}r}{\mathrm{d}t} = \epsilon \lambda_r r - \epsilon (\mu_r + \nu_r) r^3, \quad \frac{\mathrm{d}\phi}{\mathrm{d}t} = \epsilon \lambda_i - \epsilon (\mu_i + \nu_i) r^2. \tag{2.30}$$

Hence, as $\lambda_r = 9.1 > 0$ and $\mu_r + \nu_r \approx 9.1 > 0$, we have as $t \to \infty$:

$$r \to \sqrt{\frac{\lambda_r}{\mu_r + \nu_r}}, \quad \phi \sim \left(\epsilon \lambda_i - \epsilon \lambda_r \frac{\mu_i + \nu_i}{\mu_r + \nu_r} \right) t. \qquad (2.31)$$

The flow dynamics therefore converges to a limit cycle for which

$$A = \sqrt{\frac{\lambda_r}{\mu_r + \nu_r}} \exp \left[i \left(\epsilon \lambda_i - \epsilon \lambda_r \frac{\mu_i + \nu_i}{\mu_r + \nu_r} \right) t \right]. \qquad (2.32)$$

The leading part of the velocity field is therefore

$$U = U_0 + \sqrt{\epsilon} \sqrt{\frac{\lambda_r}{\mu_r + \nu_r}} \left\{ \exp \left[it \left(\omega_0 + \epsilon \lambda_i - \epsilon \lambda_r \frac{\mu_i + \nu_i}{\mu_r + \nu_r} \right) \right] U_1^A + \text{c.c.} \right\} + \cdots. \qquad (2.33)$$

We then obtain the true frequency of the bifurcated flow field on the limit cycle:

$$\omega^{LC} = \omega_0 + \epsilon \lambda_i - \epsilon \lambda_r \frac{\mu_i + \nu_i}{\mu_r + \nu_r}. \qquad (2.34)$$

The first term on the right-hand side is the frequency of the marginally stable global mode at the critical Reynolds number. The second term designates the shift in frequency due to linear mechanisms, namely the evolution of the eigenfrequency of the base-flow global mode as the Reynolds increases. The third term is a shift in frequency due to the nonlinear interactions. Numerically, we obtain

$$\omega^{LC} = 0.74 + 3.3\epsilon + 31\epsilon. \qquad (2.35)$$

This relation is sketched in figure 1(*a*) by a long-dashed line. As expected, we can see that this line is tangent to the nonlinear (experimental) curve of Williamson (1988). Incidentally, it should be emphasized that this expression invalidates the assumption of Koch (1985) and Provansal *et al.* (1987) that nonlinear terms do not influence the shedding frequency of the wake.

Note that the choice of the normalization of U_1^A yields $\lambda_r/(\mu_r + \nu_r) \approx 1$. This deeply simplifies the interpretation of the expressions involving this term. For example, the saturation amplitude r is then found to be equal to 1 and the nonlinear frequency shift reduces to $-\epsilon(\mu_i + \nu_i)$.

2.5. *Mean flow*

In this section, we introduce the mean flow associated with the periodic flow that sets in on the limit cycle. For this, recall the form of the flow field on the limit cycle:

$$U = U_0 + \sqrt{\epsilon}(A e^{i\omega_0 t} U_1^A + \text{c.c.}) + \epsilon U_2^1 + \epsilon |A|^2 U_2^{|A|^2} + \epsilon(A^2 e^{2i\omega_0 t} U_2^{A^2} + \text{c.c.}) + \cdots, \qquad (2.36)$$

where A is given by (2.32). The mean flow U^* corresponds to a time average of this expansion, that is,

$$U^* = U_0 + \epsilon \left(U_2^1 + \frac{\lambda_r}{\mu_r + \nu_r} U_2^{|A|^2} \right) = U_0 + \epsilon U_2^*, \qquad (2.37)$$

with

$$U_2^* = U_2^1 + \frac{\lambda_r}{\mu_r + \nu_r} U_2^{|A|^2}. \qquad (2.38)$$

Recall that the base flow at the Reynolds number prescribed by ϵ corresponds to $U_0 + \epsilon U_2^1$. Hence, the term $\lambda_r(\mu_r + \nu_r)^{-1} U_2^{|A|^2}$ is the difference between the mean

flow and the base flow. It corresponds to the flow field created by the nonlinear interactions. The longitudinal velocity of the mean flow u_2^* is represented by a dashed line on the symmetry plane in figure 5(*b*). We notice that this velocity is negative for $0.5 < x < 2.25$ and that it becomes strongly positive for larger values of x. Hence, recalling that the recirculation length is equal to 3.2 for the base flow U_0, it is clear that the mean flow modification both shortens and strengthens the recirculation bubble as the Reynolds number increases. This result is in accordance with the numerical and experimental observations of Zielinska *et al.* (1997) who described the mean flow in the wake of a cylinder and already stressed the role of the nonlinearities to explain its shape.

2.6. *Mean flow stability*

We now consider the linear stability of the mean flow. For this, let us introduce the following two-parameter asymptotic expansion for the flow field U valid for $0 < \epsilon \ll 1$ and $0 < \alpha \ll 1$:

$$U = U_0 + \alpha U_1 + \epsilon U_2^* + \alpha \epsilon U_3' + \cdots. \tag{2.39}$$

Here, ϵ is again the parameter controlling the Reynolds number defined in (2.2), while α is a new parameter denoting the amplitude of the critical global mode U_1. In the following, we consider very small amplitudes of this global mode which satisfy $\alpha \ll \epsilon$. Hence, the nonlinear interactions in α^2 will be negligible at order ϵ and $\alpha\epsilon$. Again, we introduce this expansion into the incompressible Navier–Stokes equations (2.1) and consider the equations at each order $\alpha^i \epsilon^j$. At order $\alpha^0 \epsilon^0$, we obtain the base flow at $Re = Re_c$. At order $\alpha^1 \epsilon^0$, we choose for U_1 the same expression as in (2.11), i.e. the critical global mode with a scalar complex amplitude A. At order $\alpha^0 \epsilon^1$, we obtain as expected that the mean flow is not a solution of the steady Navier–Stokes equations. This has been discussed by Barkley (2006). At order $\alpha^1 \epsilon^1$, we obtain a non-homogeneous linear degenerate operator for U_3':

$$(\partial_t \mathscr{L} + \mathscr{M}) U_3' = A\mathrm{e}^{i\omega_0 t} \left(-\lambda' \mathscr{L} U_1^A + F_3' \right) + \text{c.c.}, \tag{2.40}$$

with the following forcing term:

$$F_3' = \begin{pmatrix} -\nabla u_1^A \cdot \nabla u_2^* - u_2^* \cdot \nabla u_1^A - \Delta u_1^A \\ 0 \end{pmatrix}, \tag{2.41}$$

and the amplitude A depending on a slow time scale

$$\frac{\mathrm{d}A}{\mathrm{d}t} = \epsilon \lambda' A. \tag{2.42}$$

Applying the compatibility condition yields: $\lambda' = \langle \hat{U}_1^A, F_3' \rangle / \langle \hat{U}_1^A, \mathscr{L} U_1^A \rangle$. Recalling the expression of U_2^* given in (2.38), we may rewrite F_3' in the form: $F_3' = F_3^A + \lambda_r (\mu_r + \nu_r)^{-1} F_3^{A|A|^2}$. Hence,

$$\lambda' = \lambda - \frac{\lambda_r}{\mu_r + \nu_r} \mu. \tag{2.43}$$

The amplification rate and pulsation of the global mode of the mean flow are therefore given by

$$\sigma^{MF} = \epsilon \lambda_r \frac{\nu_r}{\mu_r + \nu_r}, \qquad \omega^{MF} = \omega_0 + \epsilon \lambda_i - \epsilon \lambda_r \frac{\mu_i}{\mu_r + \nu_r}. \tag{2.44}$$

Comparing these expressions to σ^{BF} and ω^{LC} in (2.28) and (2.34), we readily drew the following conclusions.

(i) If $|\nu_r/\mu_r| \ll 1$, then $|\sigma^{MF}| \ll |\sigma^{BF}|$, i.e. the mean flow is approximately marginally stable.

(ii) If $|\nu_i/\mu_i| \ll 1$, then ω^{MF} is approximately equal to ω^{LC}, i.e. the stability of the mean flow yields the nonlinear frequency of the limit cycle.

Recalling the definitions of μ and ν given in (2.24) and the definitions of $\boldsymbol{F}_3^{A|A|^2}$ and $\boldsymbol{F}_3^{\bar{A}A^2}$ in (2.17b) and (2.17c), these two conditions physically mean that the saturation process on the limit cycle is linked to the zeroth (mean flow) harmonic $\boldsymbol{U}_2^{|A|^2}$, i.e. to the nonlinear interaction of the global mode $\boldsymbol{U}_1^A$ with its conjugate $\overline{\boldsymbol{U}_1^A}$ and not to the second harmonic $\boldsymbol{U}_2^{A^2}$, i.e. the nonlinear interaction of the global mode $\boldsymbol{U}_1^A$ with itself. In the case of the cylinder, as shown by the numerical values of μ and ν given in (2.25), these two conditions are well satisfied ($|\nu_r/\mu_r| = 0.03$ and $|\nu_i/\mu_i| = 0.03$).

Alternatively, we may consider directly the numerical values of σ^{MF} and ω^{MF}:

$$\sigma^{MF} = -0.30\epsilon, \quad \omega^{MF} = 0.74 + 3.3\epsilon + 31\epsilon. \tag{2.45}$$

Recalling the numerical expression of ω^{LC} given in (2.35), we observe that $\omega^{MF} \approx \omega^{LC}$. The long-dashed line appearing in figure 1(a) therefore also represents ω^{MF}. We may conclude that mean flow stability calculations yield the true frequency of the bifurcated flow field. The relation for the amplification rate σ^{MF} appearing in (2.45) has also been sketched in figure 1(b) with a long-dashed line. We notice that this amplification rate is approximately located along the horizontal axis, i.e. the mean flow is stable, which is in accordance with the results and conclusions of Barkley (2006).

3. The case of the open cavity

The two conditions given in §2.6, i.e. $|\nu_r/\mu_r| \ll 1$ and $|\nu_i/\mu_i| \ll 1$, are the keys to justify the marginal stability of the mean flow and the relevance of its eigenfrequencies. We have tried in Appendix B to find out why this happens for the cylinder. Briefly, it turns out that this is related in part (but not mainly) to the relative strength of the zeroth (mean flow) harmonic and the second harmonic, i.e. the zeroth (mean flow) harmonic is 6.7 times stronger than the second harmonic. But a definite answer has not been obtained to explain these facts. We will show in this section that these conditions do not actually hold automatically for all globally unstable flows. For this, we give a counter-example: the open cavity.

3.1. Geometry

Let us consider an open two-dimensional square cavity of identical length and depth D. The upstream velocity U_∞ and the length D are used to make all quantities non-dimensional. The configuration and structure of the mesh is shown in figure 7. The upstream and downstream corners of the cavity are located at $(x = 0, y = 0)$ and $(x = 1, y = 0)$. The upstream boundary $\partial\Omega_1$, downstream boundary $\partial\Omega_3$ and upper boundary $\partial\Omega_4$ are, respectively, located at $x = -1.2$, $x = 2.5$ and $y = 0.5$. A uniform and unitary velocity field is prescribed at the inlet boundary $\partial\Omega_1$ at $x = -1.2$ and a laminar boundary layer starts developing on the lower boundary at $(x = -0.4, y = 0)$. A free-slip condition with zero tangential stress ($\partial_y u = 0$, $v = 0$) is prescribed on the boundaries $(-1.2 \leqslant x < -0.4, y = 0)$ and $(1.75 < x \leqslant 2.5, y = 0)$, which together form $\partial\Omega_2$. No-slip boundary conditions are imposed on $(-0.4 \leqslant x \leqslant 0, y = 0)$, on the cavity wall and on the downstream wall $(1 \leqslant x \leqslant 1.75, y = 0)$. This no-slip boundary is denoted $\partial\Omega_0$. Note that symmetry boundary conditions are used at the upper boundary $\partial\Omega_4$.
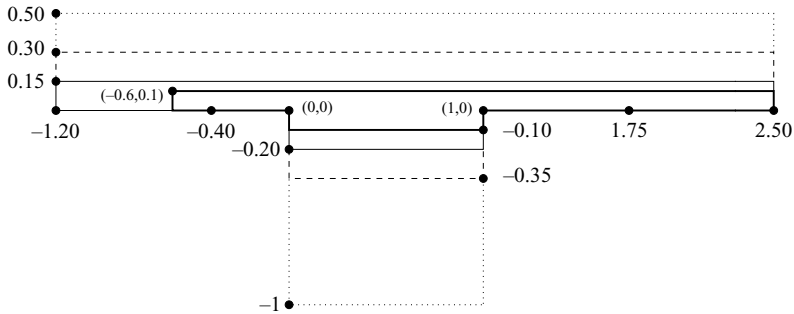
FIGURE 7. Mesh structure for the open cavity flow. The thick solid line is characterized by the vertex density n. The thin solid line, dashed line and dotted line appearing in the upper part of the mesh, i.e. in the open flow, are, respectively, characterized by the vertex densities n_1^+, n_2^+ and n_3^+. The same lines in the lower part of the mesh, i.e. in the cavity region, are, respectively, characterized by the vertex densities n_1^-, n_2^- and n_3^-.

Mesh	n	n_1^+	n_2^+	n_3^+	n_1^-	n_2^-	n_3^-	n_t	$n_{\text{d.o.f.}}$
D1	350	200	100	100	150	100	50	194771	880495
D2	500	300	150	100	200	150	100	418330	1888003

TABLE 2. Cavity flow. Different meshes used with characteristic vertex densities. D2 is much more refined than D1 and is used to test if the small-scale features of this high-Reynolds-number cavity flow are well resolved; n_t is the number of triangles, while $n_{\text{d.o.f.}}$ is the number of degrees of freedom of an unknown (u, v, p).

Concerning the structure of the mesh, the thick solid line in figure 7 is characterized by the vertex density n. The corresponding region is meshed in a very dense way in order to capture the small scales of the flow appearing there, namely the upstream and downstream boundary layers and the shear layer spanning over the cavity. The thin solid line, dashed line and dotted line appearing in the upper part of the mesh, i.e. in the open flow, are, respectively, characterized by the vertex densities n_1^+, n_2^+ and n_3^+. The same lines in the lower part of the mesh, i.e. in the cavity region, are, respectively, characterized by the vertex densities n_1^-, n_2^- and n_3^-. Two meshes denoted D1 and D2 have been used, which have the same spatial extent but different vertex densities. These vertex densities are given in table 2. Note that the vertex densities used here are much higher than those used for the cylinder case. This stems from the fact that the critical Reynolds number, as will be shown below, is nearly two orders of magnitudes higher for the cavity flow than for the cylinder flow. Hence, the structures are much smaller here and deserve more refined meshes.

In the following, all results will be presented with mesh D1. A comparison between the results obtained with D1 and D2 is offered in Appendix C.

3.2. *Base flow*

For $Re = 4140$, the base flow u_0 is represented in figure 8(a). We observe the thin free shear layer spanning over the open cavity and the large-scale recirculating flow inside it. The negative velocities inside the cavity reach $u_0 = -0.17$ near the bottom of the cavity. In figure 11(b), we have represented u_0 by a dotted line in a vertical cut localized in the middle of the cavity ($x = 0.5$, $-1 < y < 0.5$). We can see a nearly uniform flow in the region outside the cavity, a strong velocity gradient in the shear
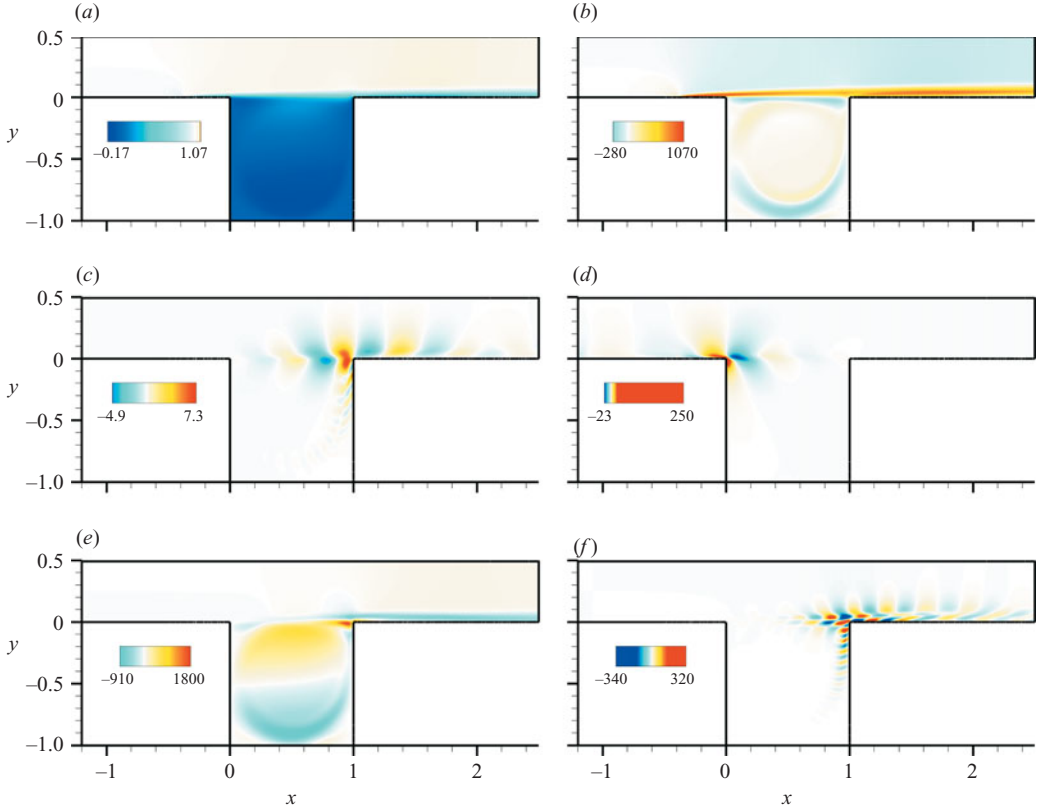
FIGURE 8. Cavity flow at $Re_c = 4140$. Mesh D1. Representation of the various flow fields appearing at each order in the weakly nonlinear analysis. (a) Base flow u_0, (b) base flow modification u_2^1 due to an increase of the Reynolds number, (c) first harmonic $Re(v_1^A)$, (d) corresponding adjoint eigenmode $Re(\hat{v}_1^A)$, (e) zeroth (mean flow) harmonic $u_2^{|A|^2}$, (f) second harmonic $Re(u_2^{A^2})$.

layer, a rigid body rotation inside the cavity, and a boundary layer on the bottom of the cavity at $y = -1$.

The characterization of the boundary layer at the upstream corner of the cavity is important for open cavity configurations. We therefore sketch in figure 9(a) the velocity profile u_0 on the vertical line $(x = 0, 0 < y < 0.5)$. The plot is focused on the high values of the velocities comprised within $0.96 < u < 1.05$. We observe a complex profile which displays a maximum $u_m = 1.039$ at $y_m = 0.0616$. Above $y > y_m$, the velocity slowly decreases and reaches the value $u_e = 1.028$ at $y = 0.5$. We notice that u_e is slightly larger than the unitary velocity imposed at the inlet boundary, indicating that a weak pressure gradient accelerates the flow in the upstream duct. This may be explained in the following manner. By incompressibility, the mean in y of the velocity field is equal to 1. Hence, as a strong velocity deficit exists in the boundary layer, the flow has to accelerate outside the boundary layer to conserve the flow rate. This is achieved by this weak pressure gradient. This mechanism is at play in the whole region outside the cavity: we observe in figure 8(a) a continuous downstream increase of the longitudinal velocities on the line $y = 0.25$. Let us now explain the existence of the observed velocity overshoot. The slow downstream thickening of the
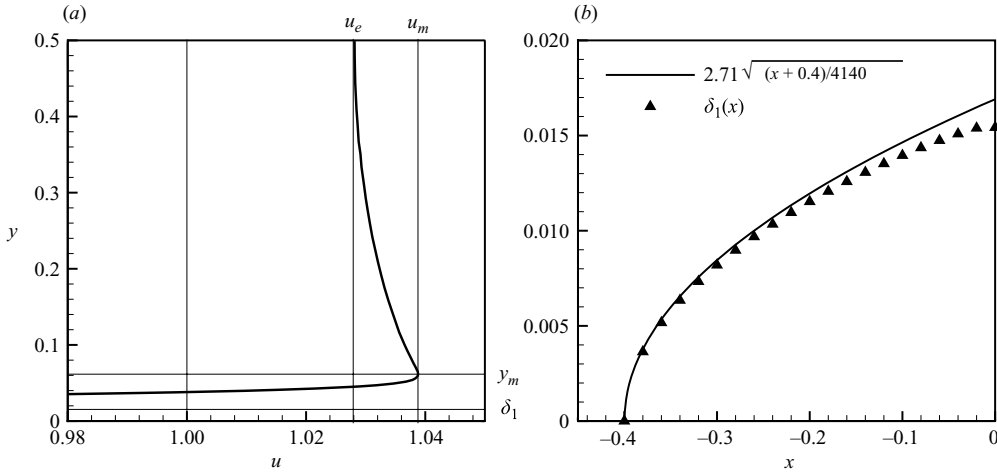
FIGURE 9. Cavity flow at $Re = 4140$. Mesh D1. (*a*) Velocity profile $u_0(0, y)$ in a vertical section localized at the upstream corner of the cavity: ($x = 0, 0 < y < 0.5$). This profile exhibits a maximum u_m at $y = y_m$. For $y > y_m$, u_0 decreases with y to reach u_e at $y = 0.5$. The boundary layer thickness δ_1 has also been shown. (*b*) The function $\delta_1(x)$ is sketched with filled triangles for $-0.4 \leqslant x \leqslant 0$, i.e. on the upstream no-slip boundary. The solid line depicts the displacement thickness of a Blasius boundary layer developing at $Re = 4140$.

boundary layer induces the existence, in the bulk of the upstream duct, of positive transverse velocities $v_0 > 0$ which decrease downstream, i.e. $\partial_x v_0 < 0$. In the case of a Blasius boundary layer, i.e. a laminar boundary layer developing with no pressure gradient for high Reynolds numbers, this transverse velocity would have been equal to $v_0 = 0.86/\sqrt{4140(x + 0.4)}$ for $Re = 4140$, which is indeed a decreasing function of x. Now, in this inviscid bulk region, by Lagrange's theorem, the vorticity of the base flow remains zero: $\xi_0 = \partial_x v_0 - \partial_y u_0 = 0$. Hence, $\partial_y u_0 < 0$ in this region, explaining the observed maximum in the velocity profile $u_0(0, y)$.

The thickness of the incoming boundary layer may be characterized on the upstream no-slip boundary $-0.4 \leqslant x \leqslant 0$ by

$$\delta_1(x) = \frac{\displaystyle\int_0^{0.5} y\xi_0(x, y)\,\mathrm{d}y}{\displaystyle\int_0^{0.5} \xi_0(x, y)\,\mathrm{d}y}; \tag{3.1}$$

$\delta_1(x)$ is a generalized displacement thickness. As a matter of fact, if the vorticity $\xi_0 \approx -\partial_y u_0$, we recover the usual definition of the displacement thickness:

$$\delta_1'(x) = \int_0^{0.5} \frac{u_e(x) - u_0(x, y)}{u_e(x)}\,\mathrm{d}y \tag{3.2}$$

where $u_e(x) = u_0(x, 0.5)$. The function $\delta_1(x)$ is sketched with filled triangles in figure 9(*b*) for $-0.4 \leqslant x \leqslant 0$, i.e. on the upstream no-slip boundary. We have also shown a relation depicting the displacement thickness of a Blasius boundary layer developing at $Re = 4140$. We observe that the two curves are similar, indicating that the present boundary layer behaves similarly to a Blasius boundary layer. Note that there is no reason that the two curves should fit exactly since the Blasius boundary layer is valid
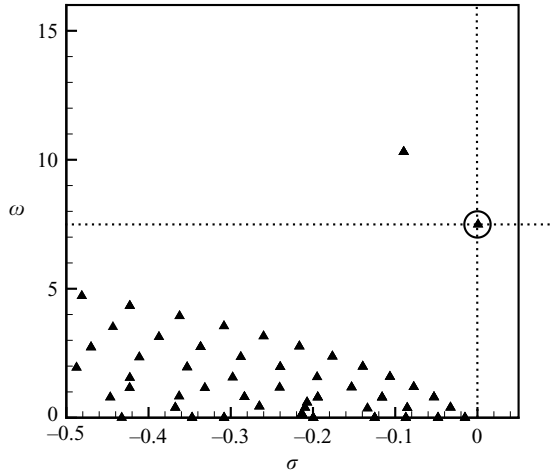
FIGURE 10. Eigenvalues of the open cavity flow in the (σ, ω) plane at $Re = 4140$. Mesh D1. A marginally stable eigenmode exists for $\omega = 7.5$ (see circled triangle).

only for $Re \rightarrow \infty$. In the present case, we obtain $\delta_1(x = 0) = 0.0153$. This value has been sketched in figure 9(*a*).

3.3. *Description of the first harmonic*

The eigenvalues of this base flow are sketched in figure 10. The eigenvalues verifying $\omega < 5$ are all stable with $\sigma < 0$. The corresponding eigenmodes are localized inside the cavity (not shown here), describing therefore the dynamics of perturbations localized in the cavity. In the region $\omega > 5$, we observe two isolated eigenmodes, one of them attenuated ($\sigma < 0$) and the other marginally stable ($\sigma = 0$). The spatial structure of the marginally stable eigenmode, characterized by $\omega_0 = 7.5$, is represented in figure 8(*c*), via its transverse velocity v_1^A. We observe that the eigenmode is localized on the free shear layer and that it consists of two vortices travelling and strengthening in the downstream direction. This may also be observed in figure 11(*a*), where the transverse velocity v_1^A has been sketched on the line $(0 < x < 1, y = 0)$ which separates the inside and outside regions of the cavity. The phase shift between the real and imaginary parts of the flow field enables a smooth downstream convection of the vortical structures. Note that we normalize here the direct and adjoint global modes by $v_1^A(0.5, 0) = 1.151$ and $\hat{v}_1^A(0.5, 0) = 1$. Comments similar to those given in §2 concerning the choice of these normalizations can be made here.

We will now repeat the steps of the weakly nonlinear analysis presented in §2. The critical eigenmode of the cavity presented above is considered in (2.11). It is therefore the first harmonic of the weakly nonlinear expansion given in (2.3).

3.4. *Description of base flow modification, zeroth and second harmonics, adjoint*

The various flow fields u_2^1, $u_2^{|A|^2}$ and $u_2^{A^2}$ have been calculated and are shown in figures 8(*b*), 8(*e*) and 8(*f*). The base flow modification U_2^1 due to the increase of the Reynolds number is spatially localized in the boundary layers and in the shear layer since the thickness of these zones diminishes with increasing Reynolds number. As a consequence, the flow acceleration existing in the region outside the cavity (described in §3.2) is diminished, which is in accordance with the negative values of the longitudinal velocity observed in this region. Also, we see that the recirculation velocities inside the cavity increase slightly.
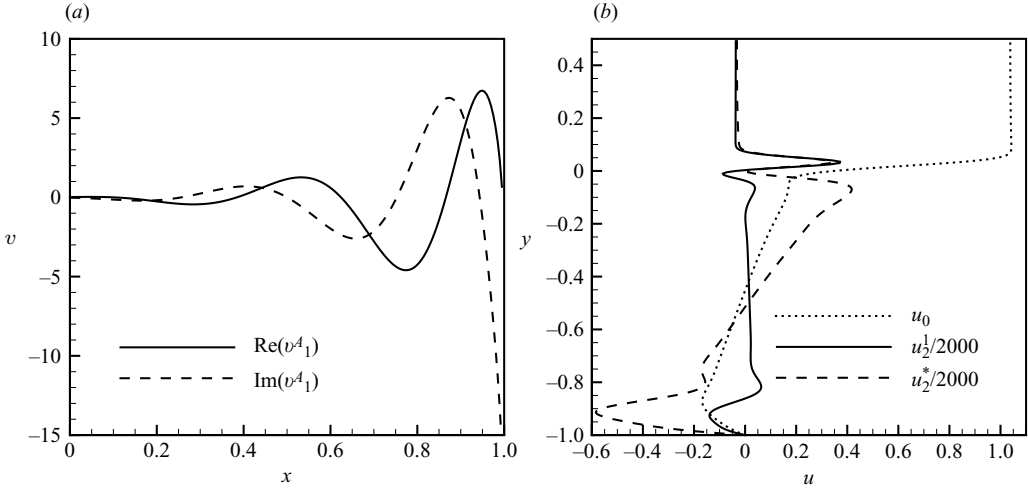
FIGURE 11. Cavity flow at $Re_c = 4140$. Mesh D1. (*a*) Real and imaginary parts of the transverse velocity v_1^A for ($0 < x < 1$, $y = 0$). The real and imaginary parts are analogous and are approximately $1/4$ spatial period out of phase, which enables a continuous downstream convection of the vortical structures. (*b*) Longitudinal velocity on ($x = 0.5$, $-1 < y < 0.5$) for the base flow u_0 (dotted line), for the base flow modification $u_2^{|A|}$ (solid line), and for the mean flow modification u_2^* (dashed line). We observe the thin free shear layer at $y = 0$, the strong velocities induced by the mean flow modification inside the cavity, while the base flow modification remains small in this region.

The zeroth (mean flow) harmonic $\boldsymbol{U}_2^{|A|^2}$ is strong in the region where the first harmonic is vigorous, i.e. in the shear layer and in the downstream boundary layer. We may also observe very high values of the recirculation velocities inside the cavity: this surprising result means that the instability developing on the shear layer has a strong nonlinear entrainment effect on the inside cavity flow field.

The second harmonic $\boldsymbol{U}_2^{A^2}$ displays small-scale structures localized near the downstream corner of the cavity.

The adjoint $\hat{\boldsymbol{U}}_1^A$ is strongly localized with very high values of the velocity on the upstream corner of the cavity. Again, we observe that the adjoint is situated upstream of the cavity while all other flow fields are localized more downstream.

3.5. *Landau constants and the limit cycle*

The numerical evaluation of (2.24) yields

$$\lambda = 3500 + 3000\mathrm{i}, \quad \mu = 2600 - 2200\mathrm{i}, \quad \nu = 890 + 180\mathrm{i}. \tag{3.3}$$

We therefore obtain for the base flow

$$\sigma^{BF} = 3500\epsilon, \quad \omega^{BF} = 7.5 + 3000\epsilon. \tag{3.4}$$

As $\lambda_r > 0$ and $\mu_r + \nu_r > 0$, following the guidelines given in §2.4.2, a saturated limit cycle exists in the case of the open cavity. This limit cycle is described by (2.33). The frequency of the flow on this limit cycle may be numerically evaluated by (2.34):

$$\omega^{LC} = 7.5 + 3000\epsilon + 2000\epsilon. \tag{3.5}$$

Comparing this relation to the base flow frequency given in (3.4), it turns out that nonlinearities strongly affect the frequency of the flow in the supercritical regime $Re > Re_c$.

3.6. *Mean flow and its stability*

The mean flow modification U_2^* may then be defined following (2.38). In figure 11(*b*), we have sketched the base flow modification u_2^1 (solid line) and mean flow modification u_2^* (dashed line) in a vertical section localized in the middle of the cavity ($x = 0.5, -1 < y < 0.5$): it is interesting to note that u_2^1 is equal to u_2^* in the external part of the free shear layer ($x = 0.5, 0 < y < 0.5$), and that u_2^* strongly affects the bulk of the cavity whereas u_2^1 is nearly zero in the area ($x = 0.5, -0.8 < y < -0.1$).

The stability of the mean flow may finally be analysed following § 2.6. Equation (2.44) yields

$$\sigma^{MF} = 900\epsilon, \quad \omega^{MF} = 7.5 + 3000\epsilon + 2200\epsilon. \tag{3.6}$$

We observe that the limit cycle frequency ω^{LC}, which was given in (3.5), is not exactly equal to ω^{MF} and that σ^{MF} is not small, i.e. the mean flow in the case of the cavity remains strongly unstable. These results are consistent with the values of the nonlinear Landau constants given in (3.3). In fact, $|\nu_r|/|\mu_r| = 0.34$ and $|\nu_i|/|\mu_i| = 0.09$ are much larger than in the cylinder case (for which $|\nu_r|/|\mu_r| \approx |\nu_i|/|\mu_i| \approx 0.03$ as shown in § 2.6). Hence, the linear stability properties of the cavity mean flow are not obvious: the mean flow is still unstable and the pulsation does not match closely the true frequency of the unsteady nonlinear flow. Hence, this is a counter-example which shows that the results obtained for the cylinder are by no means general.

4. Conclusion

We have achieved a global weakly nonlinear analysis valid in the vicinity of the critical Reynolds number Re_c based on the small parameter $\epsilon = Re_c^{-1} - Re^{-1} \ll 1$. We have computed numerically the complex constants λ, μ and ν which appear in the Stuart–Landau amplitude equation. Here λ is the linear constant leading to instability, while μ refers to the nonlinear interaction of the zeroth (mean flow) harmonic with the first harmonic and ν refers to the nonlinear interaction of the second harmonic with the first harmonic. It was shown that:

(i) If $|\nu_r/\mu_r| \ll 1$, then the mean flow is approximately marginally stable;

(ii) If $|\nu_i/\mu_i| \ll 1$, then the stability of the mean flow approximately yields the nonlinear frequency of the limit cycle.

It turns out that these conditions are well satisfied in the case of the first bifurcation occurring for the cylinder flow at $Re_c = 46.6$. This is related in part (but not mainly) to the relative strength of the zeroth (mean flow) harmonic and the second harmonic, i.e. the zeroth (mean flow) harmonic is much stronger than the second harmonic. These results give theoretical support to the numerical observations of Barkley (2006).

We have finally given a counter-example which shows that the results obtained for the cylinder are by no means general. Indeed, the two conditions mentioned above are not fulfilled in the case of an open cavity flow. Hence, generally speaking, the linear stability analyses performed on mean flows are not always meaningful. In particular, there is no reason to assume *a priori* that a mean flow is stable and that the pulsation of the mean flow matches the pulsation of the fully nonlinear flow. The two conditions mentioned above have to be checked for each globally unstable flow. To conclude, we note that the mean flow and the base flow coincide at the bifurcation, i.e. for
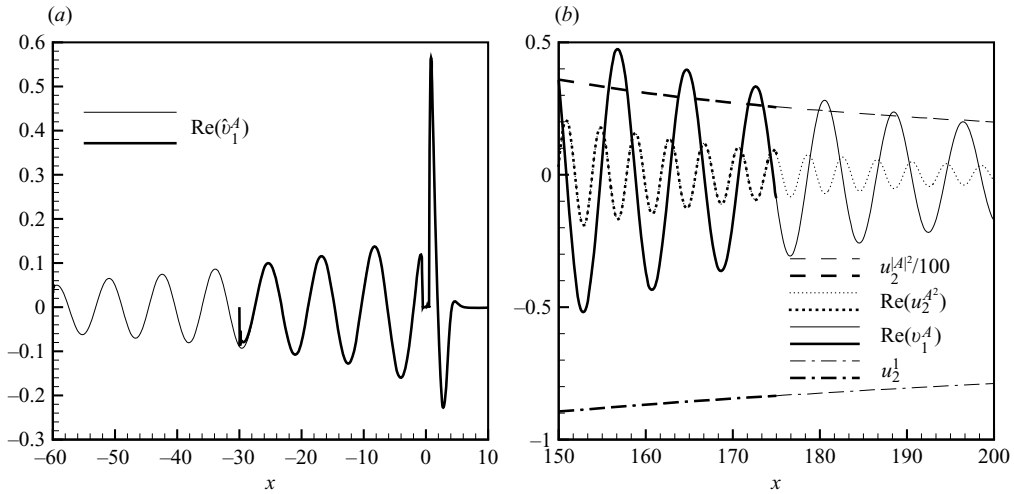
FIGURE 12. Cylinder flow at $Re_c = 46.6$. Influence of the location of the inlet and outlet boundaries. (*a*) Sketch of the adjoint transverse velocity field $\mathrm{Re}(\hat{v}_1^A)$ on the symmetry plane. The thin (respectively thick) solid line represents the solution on mesh C1 (respectively mesh C5). (*b*) Sketch of various flow fields on the symmetry plane in the downstream region $150 < x < 200$. The dashed lines represent the zeroth (mean flow) harmonic $u_2^{|A|^2}$, the dotted lines represent the second harmonic $\mathrm{Re}(u_2^{A^2})$, the solid lines the first harmonic $\mathrm{Re}(v_1^A)$ and the dash-dotted lines the base flow modification u_2^1. All thick lines (dashed, dotted, solid and dash-dotted) pertain to C4 while all thin lines are relative to C1.

critical parameters. Hence, performing stability calculations for the critical conditions guarantees in all cases the validity of linear stability analyses.

Appendix A. Comparison of results obtained with the various meshes in the cylinder case

In this section, we will show how the spatial extent of the computational domains and the vertex densities affect the results in the cylinder case.

In figure 12(*a*), we have sketched the transverse component of the adjoint flow field $\mathrm{Re}(\hat{v}_1^A)$ on the symmetry plane in the upstream region of the cylinder for mesh C1 and C5. These two meshes share identical parameters except for the location of the upstream boundary $x_{-\infty}$. For C1, $x_{-\infty} = -60$, and for C5, $x_{-\infty} = -30$. We observe discrepancies only in the range $-30 < x < -25$, i.e. the upstream boundary condition has some influence on the computed solution on a length scale of order 5. Note that a homogeneous boundary condition is applied at the inlet boundary for the adjoint flow field $\hat{U}_1^A$.

In figure 12(*b*) we have sketched, for C1 and C4 the values of $u_2^{|A|^2}$, $\mathrm{Re}(u_2^{A^2})$, $\mathrm{Re}(v_1^A)$ and u_2^1. C1 is characterized by $x_{+\infty} = 200$ and C4 by $x_{+\infty} = 175$. It appears that the position of the outlet boundary has no impact on all computed solutions.

The values of the Landau constants calculated on C1, C2, C3, C4, C5 and C6 are given in table 3. Comparing the results obtained for C1 and C4, it is obvious that the position of the outlet boundary $x_{+\infty}$ has a negligible impact. This result is in accordance with the spatial localization of the integrands involved in λ, μ and ν, and which have been given in §2.3.4. In fact, remember that the functions $\mu(x)$ and $\nu(x)$

Mesh	$10^4\sigma_0$	ω_0	λ_r	λ_i	μ_r	μ_i	ν_r	ν_i
C1	−2.241	0.73738	9.1385	3.2704	9.4529	−30.399	−0.30350	−0.86602
C2	−2.180	0.73740	9.1388	3.2593	9.4470	−30.406	−0.30312	−0.86634
C3	−1.516	0.73718	9.1386	3.2563	9.4515	−30.412	−0.30290	−0.86722
C4	−2.239	0.73738	9.1321	3.2686	9.4448	−30.400	−0.30355	−0.86358
C5	2.222	0.73907	9.1235	3.2476	9.4381	−30.007	−0.29926	−0.86455
C6	−0.036	0.73964	9.1657	3.2635	9.4344	−29.482	−0.29993	−0.86668

TABLE 3. Cylinder flow at $Re_c = 46.6$. Eigenfrequency ω_0 and Landau constants λ, μ and ν obtained for the different meshes C1, C2, C3, C4, C5 and C6 characterized in table 1. Roughly speaking, these calculations show that on nearly all constants we have three significant digits and that the location of the inlet and transverse boundaries has an influence on this third digit.

converge towards μ and ν for $x \approx 50$ and that all meshes used here extend at least up to $x = 100$. Comparing the results for C1 and C5, C1 and C6, it appears that the strongest impact stems from the positions of the upstream boundary $x_{-\infty}$ and the lateral boundary $y_{+\infty}$, which have some influence on the pulsation ω_0, and therefore on the other constants. In fact, if $y_{+\infty}$ is decreased or $x_{-\infty}$ is increased, the pulsation ω_0 slowly increases. This is due to the fact that the flow accelerates a little due to the increase of the cylinder blockage. Comparing the results from C1, C2 and C3, we can see that the vertex densities have a small impact on the obtained results. Therefore, we can conclude that we have almost three significant digits for nearly all computed constants and that the position of the upstream and lateral boundaries has an impact on this third digit.

Appendix B. Analysis of the interactions for the cylinder flow

In this appendix, we try to explain why, in the case of the cylinder flow, we have $|\nu|/|\mu| = 0.029 \ll 1$. For this, let us first define

$$\text{cs}(\boldsymbol{U}, \boldsymbol{V}) = \frac{|\langle \boldsymbol{U}, \boldsymbol{V} \rangle|}{\|\boldsymbol{U}\| \cdot \|\boldsymbol{V}\|}, \quad \|\boldsymbol{U}\| = \sqrt{\langle \boldsymbol{U}, \boldsymbol{U} \rangle}. \tag{B 1}$$

Thanks to the Cauchy–Schwarz inequality, $0 \leqslant \text{cs}(\boldsymbol{U}, \boldsymbol{V}) \leqslant 1$ for all $\boldsymbol{U}$ and $\boldsymbol{V}$. Hence, cs is a measure of the "angle" between the two vectors $\boldsymbol{U}$ and $\boldsymbol{V}$. If $\text{cs}(\boldsymbol{U}, \boldsymbol{V}) \ll 1$, then the two vectors are nearly orthogonal. In particular, this is the case when the two fields are localized in separate regions.

From the definition of μ and ν given in (2.24), it appears that

$$\frac{|\nu|}{|\mu|} = \frac{|\langle \mathscr{L}\hat{\boldsymbol{U}}_1^A, \boldsymbol{F}_3^{\bar{A}A^2} \rangle|}{|\langle \mathscr{L}\hat{\boldsymbol{U}}_1^A, \boldsymbol{F}_3^{A|A|^2} \rangle|} = \frac{\|\boldsymbol{F}_3^{\bar{A}A^2}\|}{\|\boldsymbol{F}_3^{A|A|^2}\|} \times \frac{\text{cs}(\mathscr{L}\hat{\boldsymbol{U}}_1^A, \boldsymbol{F}_3^{\bar{A}A^2})}{\text{cs}(\mathscr{L}\hat{\boldsymbol{U}}_1^A, \boldsymbol{F}_3^{A|A|^2})}$$
$$= \frac{4256}{17468} \times \frac{0.0001517}{0.001282} \tag{B 2}$$
$$= 0.24 \times 0.12 = 0.029.$$

The fact that $\text{cs}(\mathscr{L}\hat{\boldsymbol{U}}_1^A, \boldsymbol{F}_3^{\bar{A}A^2}) \ll 1$ and $\text{cs}(\mathscr{L}\hat{\boldsymbol{U}}_1^A, \boldsymbol{F}_3^{A|A|^2}) \ll 1$ may be explained in the following manner: $\hat{\boldsymbol{U}}_1^A$ is a flow field which is located upstream of the cylinder, whereas $\boldsymbol{F}_3^{\bar{A}A^2}$ and $\boldsymbol{F}_3^{A|A|^2}$ are located downstream of it, since they are built from $\boldsymbol{U}_1^A$,

Mesh	$10^4\,\sigma_0$	ω_0	λ_r	λ_i	μ_r	μ_i	ν_r	ν_i
D1	7.401	7.4930	3454.0	2991.8	2552.5	−2234.2	890.67	184.19
D2	8.961	7.4942	3452.1	2992.3	2563.5	−2233.3	887.79	185.57

TABLE 4. Cavity flow at $Re_c = 4140$. Eigenfrequency ω_0 and Landau constants λ, μ and ν obtained for the different meshes D1 and D2 characterized in table 2. Depending on the constants we have two or three significant digits.

$\boldsymbol{U}_2^{A|A|^2}$ and $\boldsymbol{U}_2^{\bar{A}A^2}$, which are all located downstream of the cylinder. Hence, the angles between these vectors are not far from being orthogonal, explaining the small values.

As seen from (B 2), the fact that $|\mu| \gg |\nu|$ stems from

$$\frac{\|\boldsymbol{F}_3^{\bar{A}A^2}\|}{\|\boldsymbol{F}_3^{A|A|^2}\|} = 0.24 \ll 1 \tag{B.3a}$$

$$\frac{\mathrm{cs}(\mathscr{L}\hat{\boldsymbol{U}}_1^A, \boldsymbol{F}_3^{\bar{A}A^2})}{\mathrm{cs}(\mathscr{L}\hat{\boldsymbol{U}}_1^A, \boldsymbol{F}_3^{A|A|^2})} = 0.12 \ll 1 \tag{B.3b}$$

The first inequality (B.3a) may be interpreted in the following manner. Recall the definitions of $\boldsymbol{F}_3^{A|A|^2}$ and $\boldsymbol{F}_3^{\bar{A}A^2}$ given in (2.17b) and (2.17c). Hence, it seems natural that:

$$\frac{\|\boldsymbol{F}_3^{\bar{A}A^2}\|}{\|\boldsymbol{F}_3^{A|A|^2}\|} \approx \frac{\|\mathscr{L}\boldsymbol{U}_2^{\bar{A}A^2}\|}{\|\mathscr{L}\boldsymbol{U}_2^{A|A|^2}\|}. \tag{B.4}$$

This may be checked numerically by noting that

$$\frac{\|\mathscr{L}\boldsymbol{U}_2^{\bar{A}A^2}\|}{\|\mathscr{L}\boldsymbol{U}_2^{A|A|^2}\|} = \frac{440}{2970} = 0.15 \approx 0.24 = \frac{\|\boldsymbol{F}_3^{\bar{A}A^2}\|}{\|\boldsymbol{F}_3^{A|A|^2}\|}. \tag{B.5}$$

Hence, the first inequality (B.3a) stems from the fact that the norm of the second harmonic is nearly an order of magnitude lower than the norm of the zeroth (mean flow) harmonic.

For the second inequality (B.3b), there is no *a priori* reason why $\mathrm{cs}(\mathscr{L}\hat{\boldsymbol{U}}_1^A, \boldsymbol{F}_3^{\bar{A}A^2}) \ll \mathrm{cs}(\mathscr{L}\hat{\boldsymbol{U}}_1^A, \boldsymbol{F}_3^{A|A|^2})$. This is obviously linked to the non-normality of the operators which separate differently in space the location of the various fields. But nothing more may be obtained from such an analysis.

Appendix C. Comparison of results obtained with the various meshes in the open cavity case

In the open cavity case, the eigenfrequencies and Landau constants have been calculated for the two meshes D1 and D2. Recall that D1 and D2 only differ by the vertex densities, which are much higher in the case of D2. Results are given in table 4. We observe differences which affect the second or third digits. We conclude that the Landau constants calculated here have two or three significant digits, depending on which constant is considered.

REFERENCES

BARKLEY, D. 2006 Linear analysis of the cylinder wake mean flow. *Europhys. Lett.* **75**, 750–756.

CHOMAZ, J.-M. 2005 Global instabilities in spatially developing flows: Non-normality and nonlinearity. *Ann. Rev. Fluid Mech.* **37**, 357–392.

DAVIS, T. A. 2004 A column pre-ordering strategy for the unsymmetric-pattern multifrontal method. *ACM Trans. Mathe. Softw.* **30**, 165–195.

DAVIS, T. A. & DUFF, I. 1997 An unsymmetric-pattern multifrontal method for sparse lu factorization. *SIAM J. Matrix Anal. Appl.* **18**, 140–158.

DING, Y. & KAWAHARA, M. 1999 Three-dimensional linear stability analysis of incompressible viscous flows using finite element method. *Int. J. Num. Meth. Fluids* **31**, 451–479.

DUSEK, J., LE GAL, P. & FRAUNIE, P. 1994 A numerical and theoretical study of the first Hopf bifurcation in a cylinder wake. *J. Fluid Mech.* **264**, 59–80.

GIANNETTI, F. & LUCHINI, P. 2007 Structural sensibility of the cylinder wake's first instability. *J. Fluid Mech.* **581**, 167–197.

HAMMOND, D. A. & REDEKOPP, L. G. 1997 Global dynamics of symmetric and asymmetric wakes. *J. Fluid Mech.* **331**, 231–260.

JACKSON, C. P. 1987 A finite-element study of the onset of vortex shedding in flow past variously shaped bodies. *J. Fluid Mech.* **182**, 23–45.

KOCH, W. 1985 Local instability characteristics and frequency determination of self-excited flows. *J. Sound Vib.* **99**, 53–83.

LE DIZÈS, S., HUERRE, P. & CHOMAZ, J.-M. 1993 Nonlinear stability analysis of slowly-varying medias: Limitations of the weakly nonlinear approach. In *Proc. IUTAM Symposium on Bluff-body Wakes, Dynamics and Instabilities*, pp. 147–152. Springer.

MONKEWITZ, P. A., HUERRE, P. & CHOMAZ, J.-M. 1993 Global linear stability analysis of weakly non-parallel shear flows. *J. Fluid Mech.* **251**, 1–20.

PIER, B. 2002 On the frequency selection of finite-amplitude vortex shedding in the cylinder wake. *J. Fluid Mech.* **458**, 407–417.

PIER, B. & HUERRE, P. 2001 Nonlinear self-sustained structures and fronts in spatially developing wake flows. *J. Fluid Mech.* **435**, 145–174.

PROVANSAL, M., MATHIS, C. & BOYER, L. 1987 Bénard–von Kármán instability: Transient and forced regimes. *J. Fluid Mech.* **182**, 1–22.

WESFREID, J., GOUJON-DURAND, S. & ZIELINSKA, B. J. A. 1996 Global mode behavior of the streamwise velocity in wakes. *J. Phys. II Paris* **6**, 1343–1357.

WILLIAMSON, C. H. K. 1988 Defining a universal and continuous Strouhal–Reynolds number relationship for the laminar vortex shedding of a circular cylinder. *Phys. Fluids* **31**, 2742–2744.

ZEBIB, A. 1987 Stability of a viscous flow past a circular cylindar. *J. Engng Math.* **21**, 155–165.

ZIELINSKA, B., GOUJON-DURAND, S., DUSEK, J. & WESFREID, J. E. 1997 Strongly nonlinear effect in unstable wakes. *Phys. Rev. Lett.* **79**, 3893–3896.